DOI 10.24425/aee.2022.142118

Consideration of the spatial orientation of magnetic field quantities and tensile mechanical stress in the Finite Element Analysis of electrical machines

BENEDIKT SCHAUERTE ✉, XIAO XIAO, KEVIN JANSEN, KAY HAMEYER

Institute of Electrical Machines (IEM), RWTH Aachen University
Schinkelstr. 4, D-52062 Aachen, Germany
e-mail: benedikt.schauerte@iem.rwth-aachen.de

(Received: 27.04.2022, revised: 15.07.2022)

Abstract: Due to speed-dependent centrifugal forces, the support of the torque, static mechanical stress introduced by manufacturing processes the laminated core of rotating electrical machines is exposed to considerable mechanical stress. The resulting stress distribution changes the magnetic properties of the electrical steel. To take this into account, a magnetization model is constituted on the basis of vector magneto-mechanical measurements that include the magnetic permeability as a function of the mechanical stress and the angle between magnetization - and the maximum principal stress direction. Subsequently, the model is integrated into the finite element simulation of a permanent magnet excited synchronous machine at different rotational speeds.

Key words: magnetic measurements, magneto-mechanical coupling vector-hysteresis, non-oriented electrical steel, Villari-effect

1. Introduction

This article is dedicated to Professor Andrzej Demenko and Professor Lech Nowak in recognition of their lifetime contribution to the field of Electric Machines.

The magneto-mechanical coupling based on the Villari-effect describes the influence of mechanical stress on the soft magnetic material properties of ferromagnetic materials [1, 2]. In the case of electrical steel, mechanical stress generally leads to a reduction in magnetic permeability and an increase in specific iron losses. In the case of unidirectional, parallel aligned magnetization and mechanical stress, the influence of compressive stress is much more pronounced than the

effects of mechanical tensile stress, which in the range of low loads up to 30 MPa even have a positive influence on the magnetic properties before the trend with increasing tensile stress reverses [3–6]. Typically, these unidirectional observations are carried out using modified single-sheet testers that are expanded with a mechanical load unit. In order to consider the magnetic anisotropy, the samples examined can be cut out at different angles to the rolling direction and placed in the magnetic sensor. A disadvantage of this procedure is the limitation to unidirectional magnetic field quantities and mechanical stress aligned only parallel to the direction of magnetization.

In order to be able to characterize the orientations between mechanical stress and magnetization in the sheet metal plane that actually occur in rotating electrical machines, different research groups have developed different sensor topologies which, in addition to the different angles between mechanical stress and magnetization, allow the impression of rotating magnetic loci [7–9]. The limiting factor in these measurement topologies, however, is the reduced, maximum possible mechanical load on the samples, which is often limited to an order of magnitude of up to 30 MPa for tensile stress and compression and is thus far below the mechanical loads that actually occur during operation.

The FE analysis performed in this work is based on the measurements of a new type of sensor topology, which represents a compromise between unidirectional characterization at high tensile stress and vectorial characterization in the limited stress range. With the help of the developed measurement system, the vectorial magnetic field quantities can be measured with one-dimensional magnetic excitation at different angles $\theta_{\sigma B}$ to the direction of tensile stress. The measurement data were used to map the magnetizability as a function of magnetic flux density B, mechanical stress σ and the angle between magnetization and mechanical tensile stress $\theta_{\sigma B}$ and transferred to the simulation as magnetic material behavior.

The material characteristic to describe the vector magneto-mechanical coupling is coupled with an a-priori mechanical stress simulation at different mechanical speed and a constant compressive pressure on the outer contour of the stator in order to be able to carry out the magneto-mechanical FE analysis. With regard to the mechanical stress distribution, only the maximum principal stress direction is considered. The transverse component of the mechanical stress is neglected for this part of the study. The resulting distribution of the magnetic flux density of the solution of a material characteristic curve without mechanical influence and a further material model based on conventional unidirectional magneto-mechanical measurement is compared.

2. Characterization of magneto-mechanical coupling

The measurement setup depicted in Fig. 1 allows the characterization of the magneto-mechanical coupling in the case of tensile stress up to the plastic deformation range.

The topology consists of the soft magnetic sample, a universal testing machine as the load unit, the rotatable magnetization yoke, a secondary coil applied on the sample and the vector hysteresis sensor attached opposite the yoke.

A 0.5 mm thick, industrially produced non-oriented electrical steel with a silicon content of 2.4% is selected as the sample-material. The sample has the dimensions of 180 mm × 60 mm. The universal testing machine loads the specimen precisely with forces of up to 20 kN, which,

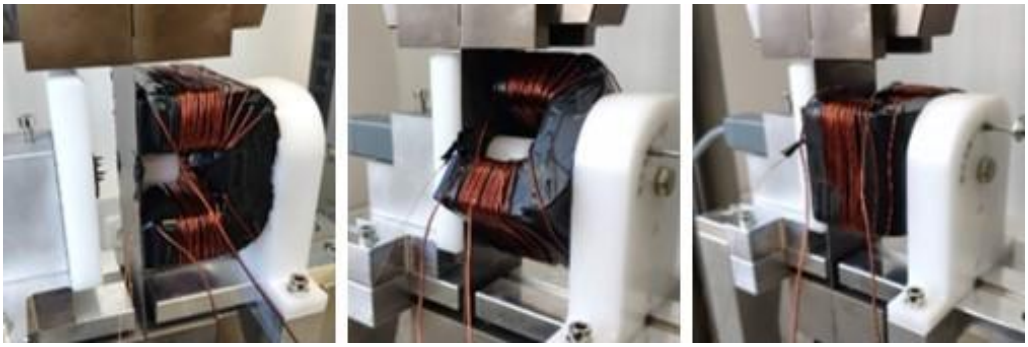

$\theta_{\sigma B} = 0°$ $\theta_{\sigma B} = 45°$ $\theta_{\sigma B} = 90°$

Fig. 1. Measurement topology with increasing angle $\theta_{\sigma B}$. Tensile stress applied in vertical direction

given the specimen dimensions, leads to theoretical mechanical stress of up to 666.67 MPa that can be applied to the specimen. Thus, the specimen can be loaded well beyond the point of plastic deformation. The magnetization yoke consists of a cut-strip wound core to which the excitation coil itself is attached. The yoke can be positioned in 15°-steps to the vertically aligned principal stress direction and thus enables the metrological characterization at different angles $\theta_{\sigma B}$. A secondary coil of two turns is attached to the sample and provides the signal for regulating a sinusoidal flux density. The vectorial magnetic field quantities and B are measured by a vector hysteresis sensor, which is pressed against the sample on the opposite side of the yoke. To prevent the sample from bending when the vector hysteresis sensor is pressed against it, there is a plastic cylinder between the two legs of the exciter yoke, which lies in a plane with the contact surfaces between the yoke and the sample.

The measurements for the construction of the vector magneto-mechanical material model were carried out at 0 and 90° between magnetization of the excitation yoke and mechanical tensile stress. The applied mechanical stress levels are 0, 10, 20, 50, 100, 150, 200, 250 and 330 MPa. One sample was characterized in each case along the rolling direction (RD) and one sample transverse to the rolling direction (TD). In this first step to set up the measurement and simulation chain for magneto-mechanical coupling with different spatial orientations, the characterization was carried out with parallel and orthogonal alignment of the magnetization to the mechanical stress at a magnetization frequency of 50 Hz, thus angles $\theta_{\sigma B}$ of 0 and 90°.

The magnetization characteristic is determined on the basis of the reversal points of the hysteresis loops of increasing maximum excitation. The measurements shown in Fig. 2 with magnetization aligned parallel to the mechanical stress are in good agreement with the material behavior measured on conventional tensile/compression SST. The measurement in RD shows a slight improvement in magnetizability for a tensile load of 10 MPa. For both orientations in relation to the rolling direction of the sample, the permeability continues to decrease with increasing mechanical load. The magnetic field strength required to achieve 1.6 T, which is less than 500 A/m in the unloaded case, increases for 330 MPa to more than 3 000 A/m. The characteristically increasing shear with increasing mechanical load can also be seen in the linear range. The measurements with orthogonal magnetization and mechanical stress depicted in Fig. 3

show a stronger influence of the mechanical stress on the magnetic permeability. For both, RD and TD, the magnetizability continuously decreases with increasing mechanical stress. Approaching the region of plastic deformation, the excitation yoke is not able to provide the required magnetic field strength beyond 6 000 A/m. For an angle $\theta_{\sigma B}$ of 90° it can be stated that the shearing of the magnetization curve is significantly stronger, than for the measurements performed at 0°.

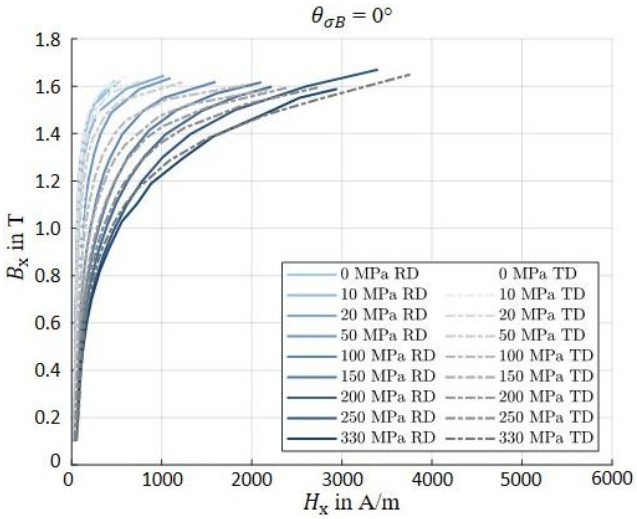

Fig. 2. Measurements for $\theta_{\sigma B} = 0°$ with increasing mechanical stress for principal stress direction parallel to RD (blue) respective TD (grey)

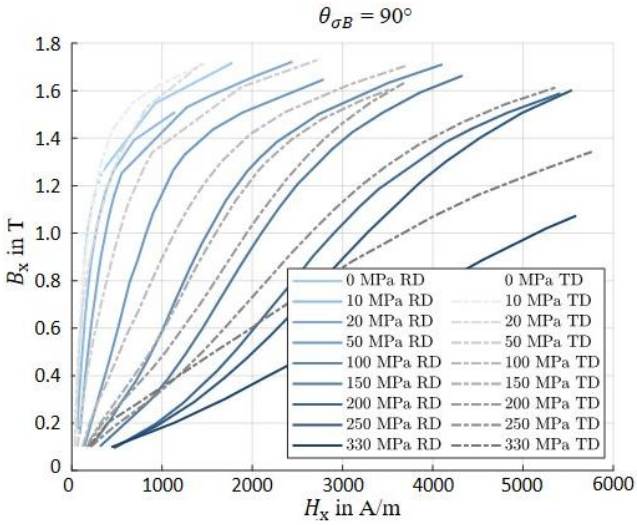

Fig. 3. Measurements for $\theta_{\sigma B} = 90°$ with increasing mechanical stress principle stress direction parallel to RD (blue) respective TD (grey)

It can be stated that the angle $\theta_{\sigma B}$ between magnetization and mechanical tensile stress has a much stronger influence on the measured material behavior than the orientation of the sample and thus also the mechanical stress to the rolling direction. The effect of magnetic anisotropy thus plays a subordinate role compared to the spatial alignment of magnetization and mechanical tensile stress.

As a consequence of this, the influence of the magnetic anisotropy is neglected in the following. After interpolation on common support points B_n, the required magnetic field strengths in RD ($H_{n,x}$) and TD ($H_{n,y}$) are averaged in order to obtain magnetization characteristics independent of the angle to the rolling direction.

3. Mechanical simulations

In order to quantify the influences of the spatial orientation of stress on the electromagnetic behavior of electrical machines, the principal stress in the electrical steel is calculated by means of a 2D finite element analysis.

The electrical machine considered in this work is a three-phase permanent magnet excited synchronous machine with 48 stator slots and eight rotor poles, which consist each of two buried permanent magnets in V-shape. In order to reduce computational effort, the symmetry unit of one fourth of the machine is chosen and simulated. For the symmetric boundary condition, frictionless support is assumed on the model boundaries. For the rotor and stator separate models are used and two exemplary sources of material stress are considered. For both the rotor and stator material Young's modulus is assumed to be 200 GPa.

For the rotor of the machine, the influence of centrifugal forces due to rotation on the material's internal stress is investigated. For that, the permanent magnets and rotor steel are modelled with a bonded connection. The permanent magnets and non-oriented electrical steel are connected both at the outward edge of the magnet pocket and the side of the magnet pocket facing towards the space between two poles. In this work a reference rotational speed of 7 500 rpm is chosen.

In Fig. 4 the resulting maximal principal stress solution is illustrated. As the influence on the electromagnetic behavior of the electrical steel is studied in this work, the principal stress solution in the permanent magnets is neglected for further evaluation.

The largest principal rotor stress amplitudes are found in the central bridges separating the magnet pockets of one pole, the outer bridges between magnet pockets and outer rotor surface and the inner transitions from the rotor yoke to the central magnet bridges. The principal stress in the rotor steel is mainly oriented in tangential direction. In the central magnet bridges, the maximum principal stress is radially oriented.

For the stator of the machine, principal stress due to pressure on the outer cylinder jacket of the stator stack is investigated. A constant pressure of 20 MPa is applied. In Fig. 6 the maximum principal stress in the stator steel is illustrated. The largest stress amplitudes are observed in the transitioning area between stator yoke and teeth. In the stator yoke, the maximum absolute principal stress is mainly oriented in tangential direction. In the stator teeth, no uniform orientation of the principal stress can be observed. Nonetheless, the absolute amplitude of the principle stress can be neglected in the stator teeth.

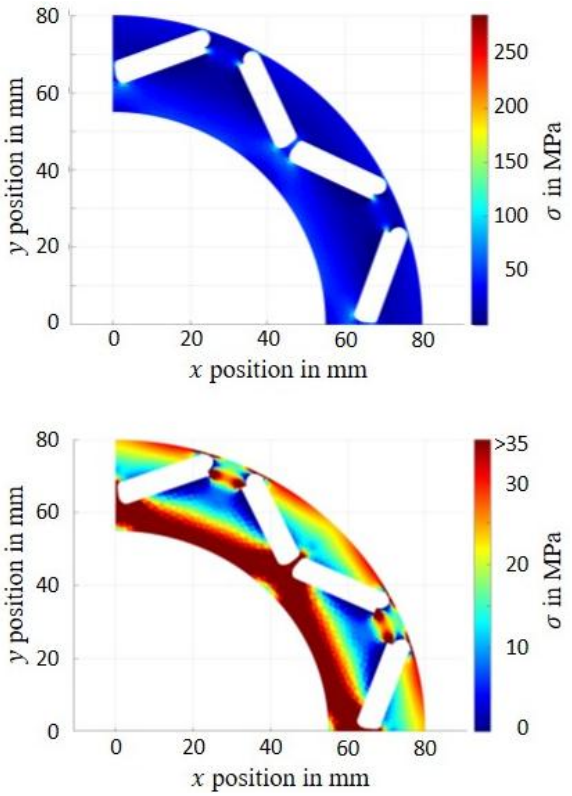

Fig. 4. Simulated mechanical stress distribution in rotor at rotational speed of 7 500 rpm depicted in two different scales

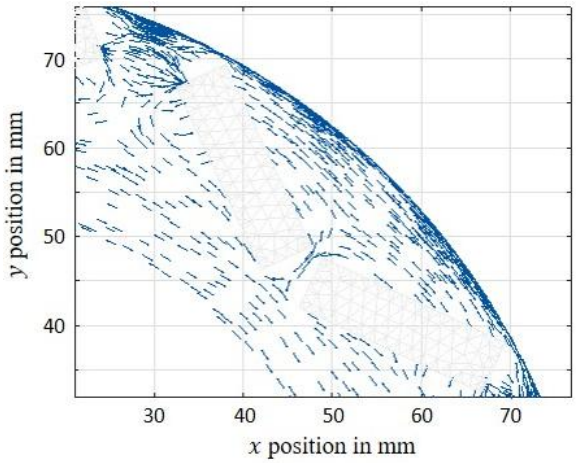

Fig. 5. Direction of principal stress in detail of rotor simulated at 7500 rpm. Length of arrows does not indicate amplitude of principle stress

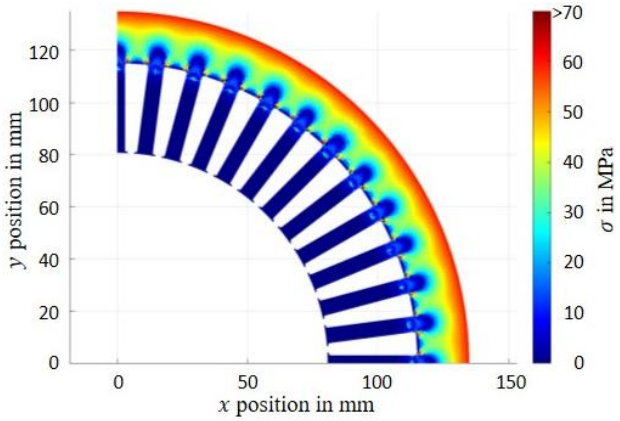

Fig. 6. Simulated mechanical stress distribution in rotor at rotational speed of 7 500 rpm

4. Incorporation of magneto-mechanical material model in 2D FE magnetic field

In this work the magneto-mechanical material model is incorporated in the 2D FE static magnetic field problem. The 2D FE method is used to predict the distribution of the magnetic flux density in the electrical motor by different operating condition with consideration of the magneto-mechanical effects impacting on the electrical steel sheet. The previously presented material model considers the dependence of magnetic properties on mechanical principal stress σ and the angle $\theta_{\sigma,B}$ between the maximum principal stress and the magnetic flux density applied to the material. With this material model the material law becomes:

$$\boldsymbol{H} = \nu \boldsymbol{B} = \nu \left(\sigma, \theta_{\sigma B}, B^2\right) \boldsymbol{B}, \tag{1}$$

where ν is the magnetic reluctivity, respectively.

The FE solver is based on the magnetostatic $\boldsymbol{A}$ formulation derived from Maxwell's equations. The magnetic vector potential $\boldsymbol{A}$ is defined with magnetic flux density $\boldsymbol{B}$ as:

$$\boldsymbol{B} = \operatorname{curl} \boldsymbol{A}. \tag{2}$$

Applying the material model (1) and the Coulomb gauge condition to Eq. (2) to ensure a unique magnetic vector potential $\boldsymbol{A}$ defined in the domain Ω, the equation becomes

$$\operatorname{curl} \nu \left(\sigma, \theta_{\sigma B}, B^2\right) \operatorname{curl} \boldsymbol{A} = \boldsymbol{j}, \tag{3}$$

where $\boldsymbol{j}$ represents the imposed steady currents and the remanence induction.

The weak formulation of the magnetostatic problems of Eq. (3) can be written with integral of the scalar product as:

$$\left(\nu \left(\sigma, \theta_{\sigma,B}, B^2\right) \operatorname{curl} \boldsymbol{A}, \operatorname{curl} \boldsymbol{A}'\right)_{\Omega} + \langle \boldsymbol{n} \times \boldsymbol{h}_s, \boldsymbol{A}' \rangle_{\Gamma_h} = (\boldsymbol{j}, \boldsymbol{A}')_{\Omega} \ , \tag{4}$$

where Ω is the set of the Euclidean space, Γ_h is the part of the boundary, $\boldsymbol{h_s}$ is the source term related to the $\boldsymbol{j}$ and $\boldsymbol{A'}$ is the test function. Using the Galerkin method to choose the test function $\boldsymbol{A'}$ as the same as the basis function $\boldsymbol{A} = \sum_{i=1}^{N} A_i \boldsymbol{\alpha_i}$ in the approximated spatial discretization space of Ω.

As the magnetic vector potential formulation is coupled with the nonlinear material model, the field problem is solved in this work by means of the Newton method. The equation system starting from its Taylor series first order of the timestep t yields [10]:

$$[\boldsymbol{J}]_k \left(\boldsymbol{A}_{k+1} - \boldsymbol{A}_k\right) = [\boldsymbol{R}]_k \,, \tag{5}$$

where the Jacobian matrix $\boldsymbol{J}$ and the residuum vector $\boldsymbol{R}$ of the iteration k can be written as:

$$\boldsymbol{J}_{ij} = \left(\frac{\partial \boldsymbol{H}}{\partial \boldsymbol{B}} \cdot \operatorname{curl} \alpha_i^T \,,\, \operatorname{curl} \alpha_j\right)_\Omega \,, \tag{6}$$

$$R_i = \left(\boldsymbol{H}(\boldsymbol{B}) \cdot \operatorname{curl} \alpha_i^T - j\alpha_i\right)_\Omega \,. \tag{7}$$

In the scalar case, the differential reluctivity matrix $\boldsymbol{\nu_d} = \dfrac{\partial \boldsymbol{H}}{\partial \boldsymbol{B}}$ can be calculated with Eq. (8):

$$\frac{\partial \boldsymbol{H}}{\partial \boldsymbol{B}} = \frac{\partial \nu\left(\sigma, \theta_{\sigma,B}, B^2\right)}{\partial \boldsymbol{B}^2} 2\boldsymbol{B}^2 + \nu\left(\sigma, \theta_{\sigma,B}, B^2\right). \tag{8}$$

Therefore, the material model needs to provide for each newton iteration in each timestep for each element the derivative value $\dfrac{\partial \nu\left(\sigma, \theta_{\sigma,B}, B^2\right)}{\partial \boldsymbol{B}^2}$ and $\nu\left(\sigma, \theta_{\sigma,B}, \boldsymbol{B}^2\right)$ according to σ on the element and the angle $\theta_{\sigma B}$ between the main principal stress direction σ and the magnetic flux density $\boldsymbol{B}$ on this element. This is achieved by means of cubic spline interpolation from the surfaces, as shown in Fig. 7, constructed by the magneto-mechanical material model. These surfaces together with a .txt-file are as data base imported into the solver. The .txt-file contains the information of element numbers, the corresponding principal stress and the respective angle, which simulated from the Section 3 for the electrical steel sheets considering the mechanical effects.

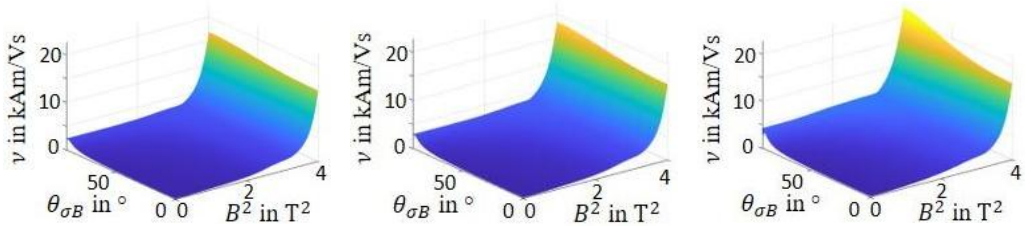

(a) σ = 200 MPa (b) σ = 250 MPa (c) σ = 330 MPa

Fig. 7. Bridge voltage, bridge voltage after-rectification and phase current waveforms of the three-level T-type inverter under normal and fault conditions: S_{a1} open-circuit fault (a); S_{a2} open-circuit fault (b); phase-leg fault in phase-a (c)

For the first iteration $k = 1$ of each time step in the Newton scheme, the initial node solution $\boldsymbol{A}_{t,k=1}$ is set as the solution from the last time step $\boldsymbol{A}_{t-1,k=n}$.

To ensure the convergence of the Newton method, the ν surfaces under one certain angle and principal stress orientation versus the increasing $\boldsymbol{B}^2$, as shown in Fig. 7, must be monotonic increasing. The convergence of the iteration schemes is reached at all the time steps with a relative tolerance by 10^{-5}.

5. Results

The primary principle mechanical tensile stress and the respective direction are assigned to each element of the mechanical machine model for the electromagnetic simulation. Look-up tables are stored in the form of the surfaces of the magnetic reluctance to take the material behavior into account during the FE calculation.

In order to assign a mechanical stress and the angle of the maximum principle direction to each element of the electromagnetic machine model according to the simulation results of the mechanical simulation, the geometric center of gravity of each element is calculated. Since the elements of the electromagnetic machine model have the shape of triangles, the geometric center of gravity for each element is calculated as follows:

$$x_\mathrm{s} = \frac{(x_\mathrm{a} + x_\mathrm{b} + x_\mathrm{c})}{3}, \tag{9}$$

$$y_\mathrm{s} = \frac{(y_\mathrm{a} + y_\mathrm{b} + y_\mathrm{c})}{3}, \tag{10}$$

where x, $y_{\mathrm{a,b,c}}$ are the coordinates of the nodes and x, y_s are the coordinates of the center of gravity for each element.

To test the convergence of the FE- and material model a of three operation points defined by three different rotational speeds (2 500, 5 000 and 7 500 rpm) and a torque of 200 Nm were simulated. So as not to go beyond the scope of this paper, only the results of the simulation carried out for 7 500 rpm are shown below, in which the centrifugal forces in the rotor are at their maximum and thus exert the greatest influence on the magnetic flux distribution. According to the selected operation point, the simulation was assigned the current combination of $I_\mathrm{d} = -281.69$ A and $I_\mathrm{q} = 120.62$ A.

With the current measurement setup, only tensile stress can be characterized. However, especially in the pressed-in stator, compressive stress mainly occurs in many areas. In order to be able to incorporate the known much stronger influence of compressive stress in this first attempt of the measurement and simulation chain, the respective elements were assigned the tensile stress multiplied by a factor of three.

The consideration of the resulting flux density distributions shown in Fig. 8–10 and the calculated difference show a considerable influence of the mechanical stress. The greatest reduction in the magnetic flux density can be seen at the edges of the outer edges of the V-shaped buried magnets. In combination with the orientation of the maximum principle stress shown in Fig. 5, it can also be explained why the magnetic flux runs in less circular flux lines between the permanent magnets of two poles. The magnetic resistance is highest at an angle of 90° between the principal

mechanical stress direction and magnetization. Since the principal stress in the interior of the laminated rotor core run radially, the magnetic flux emerging from the permanent magnets is also forced in this direction due to the magnetic resistance. Thus, in comparison to the reference simulation, there is a displacement of the magnetic flux from the inner contour of the rotor to the direct, tangentially aligned connections between the magnets of the respective poles.

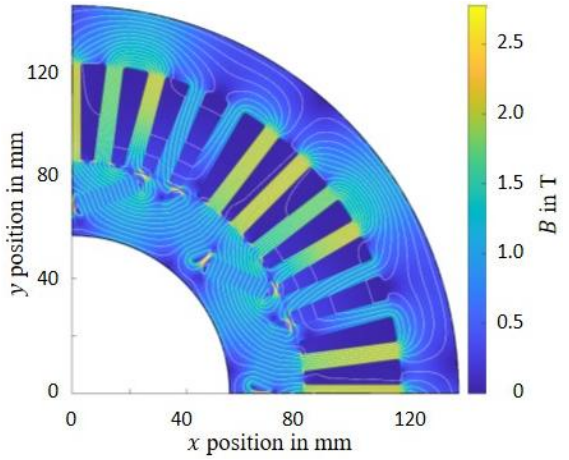

Fig. 8. Reference simulation. Flux density distribution for one-dimensional magnetization curve without influence of mechanical stress

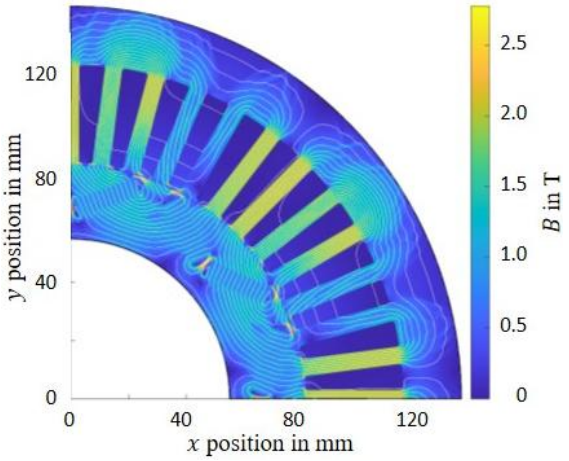

Fig. 9. Resulting flux density distribution under consideration of spatial orientation of principal stress and magnetization

In the thin webs, however, the influence of the magneto-mechanical coupling is almost invisible, since these areas are very heavily saturated by the leakage flux. In the area of such inductions,

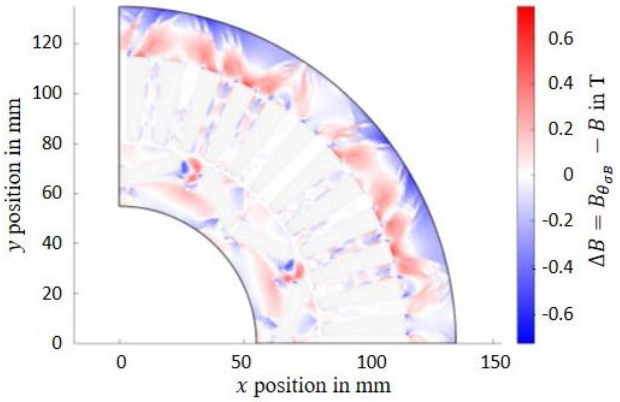

Fig. 10. Difference between simulations with and without consideration of spatial orientation of principle mechanical stress and magnetization. Color red indicates an increased flux density in comparison to reference simulation

the magneto-elastic effect continues to lose its influence, so that the simulation here is in good agreement with the theory.

In the area between the permanent magnets and the air gap, the overall picture is less uniform. The principal stress in this area are also oriented more tangentially after a spatially limited transition from the thin webs, and thus orthogonally to the magnetization. Due to the offset angle between the rotor position and the stator field, the flux density is concentrated here on the area on the right when viewed from the inside. Since the flux strives to align itself along the orientation of the mechanical stress, just like along the inner contour, the flux here is pushed from the weaker magnetized area of the left permanent magnet into the already more strongly magnetized area of the magnet on the right side of the V-shape.

The effects of the magneto-mechanical coupling can also be seen very clearly in the stator. Similarly to the inner contour of the rotor, the magnetic flux is displaced in the stator yoke away from the outer contour in the direction of the origin of the stator teeth. Especially for the neighboring teeth with low levels of magnetization, a very strong increase in the magnetic flux density can be observed along the inner contour of the stator.

The flux lines depicted in Fig. 9 for the simulation considering the magneto-mechanical coupling, show in the stator yoke a highly irregular course due to the mechanical stress distribution in this area, which is oriented in the radial direction. It is questionable whether the course of the field lines actually has such an irregular shape. To assess this point, further measurements at angles $\theta_{\sigma B}$ between 0 and 90° are necessary to confirm the elliptical approach chosen in this work.

The irregular pattern in the stator teeth is due to the very low mechanical stress levels that the mechanical simulation correctly supplies here, but which vary strongly in their respective orientation. Due to the measurement setup, there is a very strong directional dependence of the magnetization in the area of low magnetization, which is reproduced in these areas of strongly fluctuating angles $\theta_{\sigma B}$.

6. Conclusions

In this work, the spatial vector magneto-mechanical coupling was studied by means of measurements with parallel and orthogonally oriented mechanical tensile stress and magnetizations. The measurement results were transferred to the FE analysis of an eight-pole PMSM using an elliptical approach depending on the magnetic flux density B, the mechanical stress σ and the angle between magnetization and the principal mechanical stress $\theta_{\sigma B}$. The measured strong influence of the magneto-mechanical coupling was strongly reflected in the distribution of the magnetic flux density of the electrical machine.

A simulation based on a single magnetization curve was used as a reference without considering the mechanical stress and its influence on the magnetic behavior. The measurement and simulation chain have been successfully established, nonetheless this study is influenced by various simplifications.

The mechanical stress distribution was only considered with regard to the principal stress of the first order. The case of shear and considerably high secondary principal stress has not yet been measured and considered in the material model. In addition, vector magneto-mechanical measurements under the influence of compressive stress have to be performed in order to include this stress state in the material model based on measurement results.

In the future, measurements will be performed at angles $\theta_{\sigma B}$ between 0 and 90° for both tensile and compressive stress to be carried out in order to be able to validate the elliptical approach chosen as a first approximation on the basis of measurement results and to be able to adapt it further to the measurement results.

Acknowledgements

This work was supported by the Deutsche Forschungsgemeinschaft (DFG) in the DFG priority program "SPP2013 – Focused Local Stress Imprint in Electrical Steel as Means of Improving the Energy Efficiency" – HA 4395/22-1.

References

[1] Bozorth R.M., *Ferromagnetism* (1993).

[2] Cullity B.D., Graham C.D., *Introduction to magnetic materials*, John Wiley & Sons (2011).

[3] Leuning N., Steentjes S., Hameyer K., *Effect of magnetic anisotropy on Villari Effect in non-oriented FeSi electrical steel*, International Journal of Applied Electromagnetics and Mechanics, vol. 55, no. S1, pp. 23–31 (2017).

[4] Karthaus J., Elfgen S., Hameyer K., *Continuous local material model for the mechanical stress-dependency of magnetic properties in non-oriented electrical steel*, COMPEL-The International Journal for Computation and Mathematics in Electrical and Electronic Engineering (2019).

[5] Lahyaoui O., Lanfranchi V., Buiron N., Martin F., Aydin U., Belahcen A., *Effect of mechanical stress on magnetization and magnetostriction strain behavior of non-oriented Si-Fe steels at different directions and under pseudo-DC conditions*, International Journal of Applied Electromagnetics and Mechanics, vol. 60, no. 2, pp. 299–312 (2019).

[6] Singh D., Rasilo P., Martin F., Belahcen A., Arkkio A., *Effect of mechanical stress on excess loss of electrical steel sheets*, IEEE Transactions on Magnetics, vol. 51, no. 11, pp. 1–4 (2015).

[7] Aydin U., Rasilo P., Martin F., Belahcen A., Daniel L., Haavisto A., Arkkio A., *Effect of multi-axial stress on iron losses of electrical steel sheets*, Journal of Magnetism and Magnetic Materials, vol. 469, pp. 19–27 (2019).

[8] Kai Y., Tsuchida Y., Todaka T., Enokizono M., *Measurement of the two-dimensional magnetostriction and the vector magnetic property for a non-oriented electrical steel sheet under stress*, Journal of Applied Physics, vol. 111, no. 7, 07E320 (2012).

[9] Permiakov V., Pulnikov A., Dupre L., Melkebeek J., *Rotational magnetization in nonoriented Fe-Si steel under uniaxial compressive and tensile stresses*, IEEE Transactions on Magnetics, vol. 40, no. 4, pp. 2760–2762 (2004).

[10] Bouillault F., Kedous-Lebouc A., Meunier G., Ossart F., Piriou F., *The finite element method for electromagnetic modeling*, John Wiley & Sons, Ltd., Chapter 5, pp. 177–244 (2010).